DE GRUYTER Open Geosciences 2021; 13: 1328–1344

Research Article

Amr Abd El-Raouf*, Ibrar Iqbal, Julia Meister, Kamal Abdelrahman*, Hassan Alzahrani, and Osman M. Badran

Earthflow reactivation assessment by multichannel analysis of surface waves and electrical resistivity tomography: A case study

https://doi.org/10.1515/geo-2020-0310
received August 03, 2021; accepted October 24, 2021

Abstract: In this study, we investigated the stability and reactivation of preexisting Tonghua landslide deposits in China, including the adjacent stable slope. We used an integrated approach, combining a multichannel analysis of surface waves (MASW) and electrical resistivity tomography (ERT). We used ERT to determine groundwater seepage paths, weathering conditions, water content, and the depth to bedrock. High-resolution two-dimensional (2D) shear-wave velocity MASW images, on the other hand, played an essential role in detecting both horizontal and vertical compositions, disjointedness, and sliding surfaces related to lithological borders. Based on seismic models, we considered four geological layers encountered in the stable slope, including fractured (gravel) and weathered (phyllite) materials, as a sliding mass. We combined the 2D resistivity profiles obtained to create pseudo-three-dimensional ERT images to estimate water-saturated and unsaturated masses. From the tomography results, we identified different preexisting deposits, including buried arable clay deposits, old accumulated earthflow deposits, a water accumulation zone, and a fissure runoff. Based on the resistivity results, the bottom of the earthflow deposits is susceptible to water, and oversaturation can reactivate the earthflow.

Keywords: earthflow, geophysical approach, electrical resistivity tomography, pseudo-3D survey, multichannel analysis of surface waves, noninvasive

1 Introduction

Natural disasters frequently cause severe hazards to thoroughfares and transport substructures, homes, industrial facilities, and utilities. Landslides are natural hazards that can occur anywhere worldwide. According to the Chinese Ministry of Land and Resources, from 2001 to 2010, 9,941 people died or disappeared in disastrous events such as landslides and mudslides. Furthermore, 25,000 deaths were recorded due to landslides, collapses, and mudslides on December 05, 2008 resulting from the Wenchuan earthquake in China [1]. A reason for such events at the southeast brink of the Tibetan level is the collision of the Indian and Eurasian plates, which causes significant active faults and complex geological tectonics. Tens of thousands of shattered gradients and coseismic mudslide deposits have also become more susceptible to storms and rainfall due to seasonal changes. Extreme rainfall, for instance, can cause water to infiltrate into shear ruptures or creep–tensile ruptures, resulting in instability. It can also increase orifice water pressure and decrease the significant trimming resistance of a subsurface sliding surface [2,3]. Thus, it is vital to assess the sliding material thickness, locate subsurface sliding surfaces, and to differentiate the groundwater spread within landslide events to evaluate hazard prevention processes [4–6].

Geophysical tools, geotechnical approaches, and remote sensing and airborne techniques are used in assessing

---

*** Corresponding author: Amr Abd El-Raouf,** Geology Department, Faculty of Science, Zagazig University, Zagazig 44519, Egypt; School of Earth Sciences, Zhejiang University, Zheda Road 38, Hangzhou 310027, China, e-mail: ammohammed@science.zu.edu.eg
*** Corresponding author: Kamal Abdelrahman,** Department of Geology and Geophysics, College of Science, King Saud University, P.O. Box 2455, Riyadh 11451, Saudi Arabia, e-mail: khassanein@ksu.edu.sa
Ibrar Iqbal: College of Geosciences, Guilin University of Technology, Guilin, 541004, Guangxi, China
Julia Meister: Institute of Geography and Geology, Chair of Physical Geography, University of Würzburg, Am Hubland, 97074 Würzburg, Germany
Hassan Alzahrani: Department of Geology and Geophysics, College of Science, King Saud University, P.O. Box 2455, Riyadh 11451, Saudi Arabia
Osman M. Badran: Geology Department, Faculty of Science, Damanhour University, El-Gomhouria St, Damanhour 22511, Egypt

landslide hazards. Geophysical approaches to landslide analysis that can help determine the physical properties directly and indirectly associated with mass movements. These tools are attractive as they are inexpensive, rapid, and noninvasive means to assess slopes and landslide areas [7].

Drilling assays for geotechnical assessment on unstable slopes are unsafe and expensive. It is difficult to drill boreholes in the main body of landslides owing to inherent instability. However, employing surface geophysical methods can reduce the number of drilled holes required in landslide sites [8,9]. Incorporating geophysical testing techniques can reduce indecision in reverse models and let each technique compensate for the fundamental disadvantages of the others. Therefore, the use of a combination of geophysical methods is highly recommended. The most widely used geophysical approaches for assessing landslides are multichannel analysis of surface waves (MASW) and electrical resistivity tomography (ERT) [10,11]. They can clarify geological characteristics with more reliable and precise models [12]. Used together, they provide remarkably reliable assessments in regions with high water content [13–16].

In landslides, the geophysical properties of depositional patterns comprise factors such as soil type, porosity, saturation level, stress status, soil thickness, and bedrock type. These factors control the electrical and seismic responses of rock and sediments. Therefore, geophysical investigations are dependable for assessing and predicting the landslides from an engineering perspective. Interpretation of geophysical data has proved the utility of geophysical methods of landslip inquiries to identify the position of the collapse zone, angle morphology (scarps, flanks, and toe bulges), differences in lithology and soil types, moisture systems, and fluctuation in water over time [7,17–23].

Herein, the Tonghua landslide site in China (situated at 31°34′25.49″, 103°24′58.92″), which comprises a translational landslide at an elevation of 2,030 m above the Zagunao River (Figure 1), was used as a case study. Its first downslope movement was reported on August 11, 2017. Its triggering factor was connected to heavy precipitation between June and July 2017. The downslope movement was reactivated on August 15, 2017, which continued until September 07, 2017 (Figure 2).

This site still experiences constant slow-shifting landslides caused by precipitation in the region. Climate change, which modifies both the regularity and scale of rainfall, can significantly impact landslide reactivation. This may happen along with extreme earthquake events, which may cause slow-shifting landslides to develop into a copious rubble stream with a lengthy runout [6]. This is a crucial observation, which causes uneasiness as the municipality of Tonghua is situated downhill from this landslide. A repetition of this landslide would pose a risk to hundreds of people, the town's infrastructure and 20 km secondary roads, and the adjacent Zagunao River.

To date, geotechnical and meteorological studies on the causes of landslides have been reported [6], but only a few studies have used geophysical approaches to explore the inner features of slope failures in the Tonghua landslide region. In this study, we combined ERT and MASW, which allow frequent hydrological and geotechnical investigations and subsurface characterization of the main landslide body. This approach could identify the inner composition, especially possible slipping surfaces, to determine the stability of the structures and predict the role of water in the reactivation of preexisting landslide debris.

2 Methods

2.1 Geomorphological and geological setting

The Tonghua landslide occurred near the Xishan village of Tonghua, Northwest Sichuan Province, China. The typical elevation is approximately 2,300 m, with high mountains and deep valleys in the case-study region. Denudation of vegetation in the region is very high, and the terrain is mostly alpine [24]. A portion of the interim belt extends from the eastern edge of the Qinghai–Tibet plateau to the east Sichuan bowl. Historic earthquakes strongly influence the slope structures of the area; thus, the landslide risk factors are high and may cause safety issues in the future. The most active slope segments in the area are the bulged portions, ranging from 30 to 40°. Ancient superficial deposits on the surface of the slopes include the Devonian system and Quaternary deposits. The basis is generally Devonian crystals containing phyllite and Holocene colluvial deposits [24].

The landslide body is, thus, stratigraphically associated with the collection of Quaternary glacial deposits. The fourth and fifth parties of the Silurian Maoxian establishment control visible divisions in this area (Figure 3), which mainly include metamorphic pillars and diverse deposits of loose sediments. The lithology comprises limestone, sandy slate, phyllite, and metamorphosed stone. The varied deposits of loose sediments are predominantly

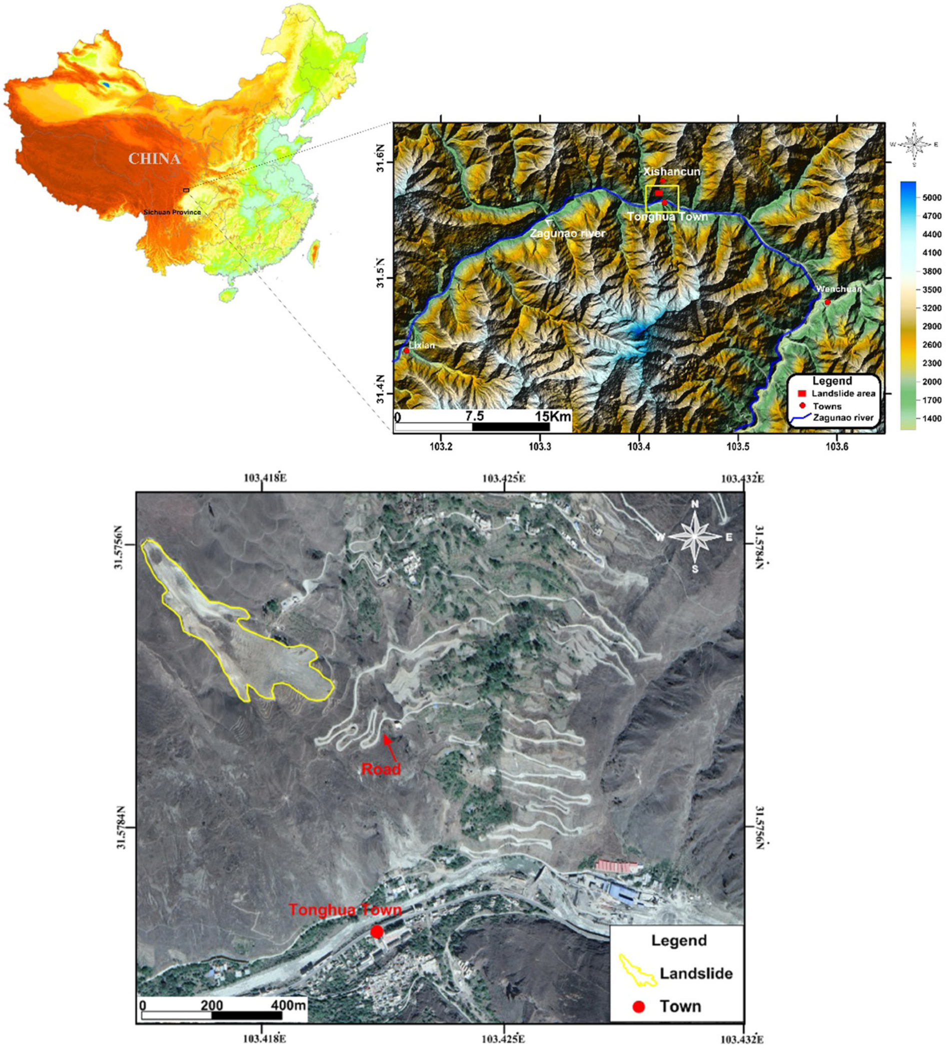

Figure 1: The digital elevation map of the landslide area around the Zagunao River and the investigated Tonghua landslide site near Xishan village.

categorized into three: (i) glacial deposits, (ii) alluvial deposits, and (iii) colluvium. Glacial deposits form a unique residue landform in this region.

Different geotechnical reports have described the lithology of the various layers. The first layer comprises pebbly clay layers composed of breccia and gravels ranging from 2 to 20 mm. This layer contains 75% clay, making it highly plastic. The second layer, which is gravelly soil, consists of more than 50% gravel ranging from 10 to 50 mm and sand ranging from 0.5 to 2.0 mm. The parent rock is phyllite, and the weathering rate is high. The third layer of the Zagunao River deposits comprises Quaternary alluvial sediments. Large-scale joint fissures with potential flow paths and transportation were first reported in ref. [25], and a dendritic pipe-network seepage system was later identified and categorized in the region [24]. Figure 3(b) shows the borehole lithological log according to previous drill boreholes [24]. The shallow subsurface succession consists of Quaternary diluvium, gravel clay soil, gravel soil, solidly endured phyllite, weathered phyllite, and phyllite bedrock respectively from the top to bottom.

Structurally, the study area is near the Longmenshan fault belt. As shown in Figure 4, the tectonic block is very active and has caused several earthquakes [6]. The China Seismic Network database shows that from 2012, the region within 30 km of the Tonghua landslip has been influenced by more than 28 seismic incidents of surface wave magnitude (Ms) ≥3. Notably, the integrity of the collapsed area was brutally broken by the 2008 Wenchuan Ms-8.0 earthquake as the locale of the landslip is only 66 km from the epicenter of the earthquake. Furthermore, there has been a giant prospective landslide,

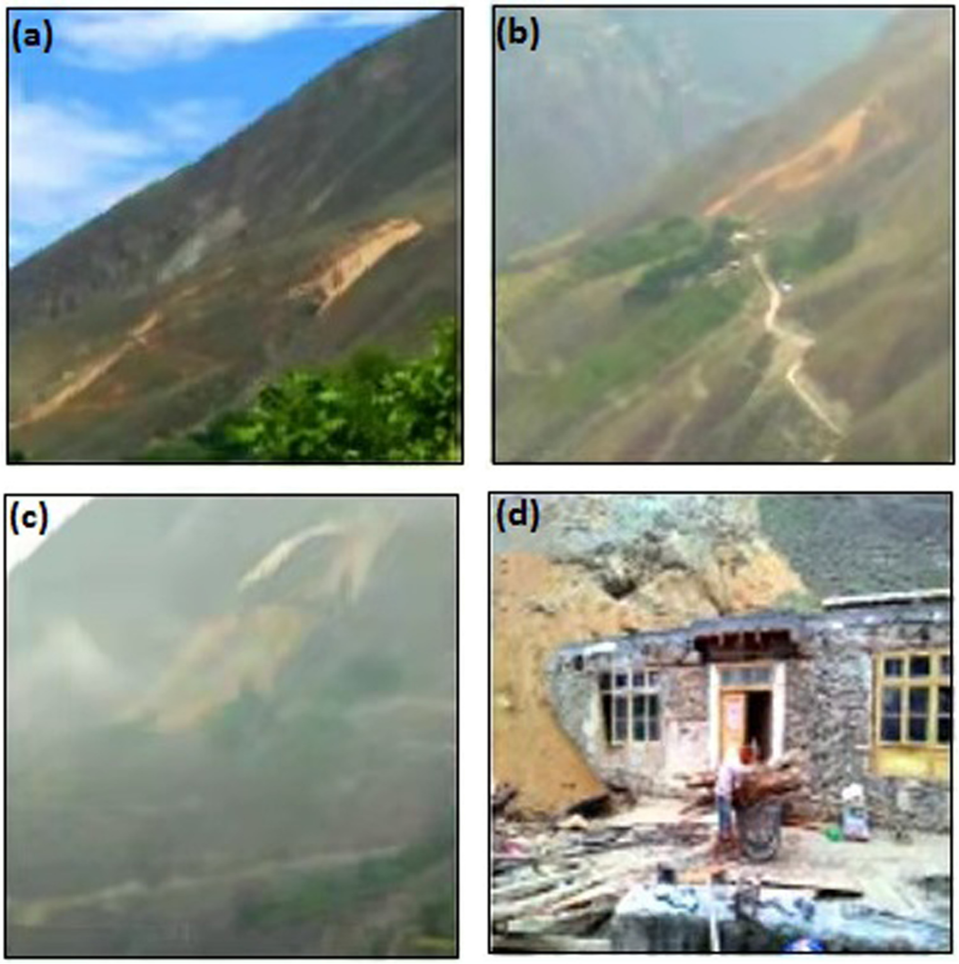

Figure 2: Landslide failure surface at Tungua landslide: (a) the initial failure on August 11, 2017; (b) the reactivation took place on 15 August; (c) continuous catastrophic movement until September 7, 2017, and (d) evacuation of local houses.

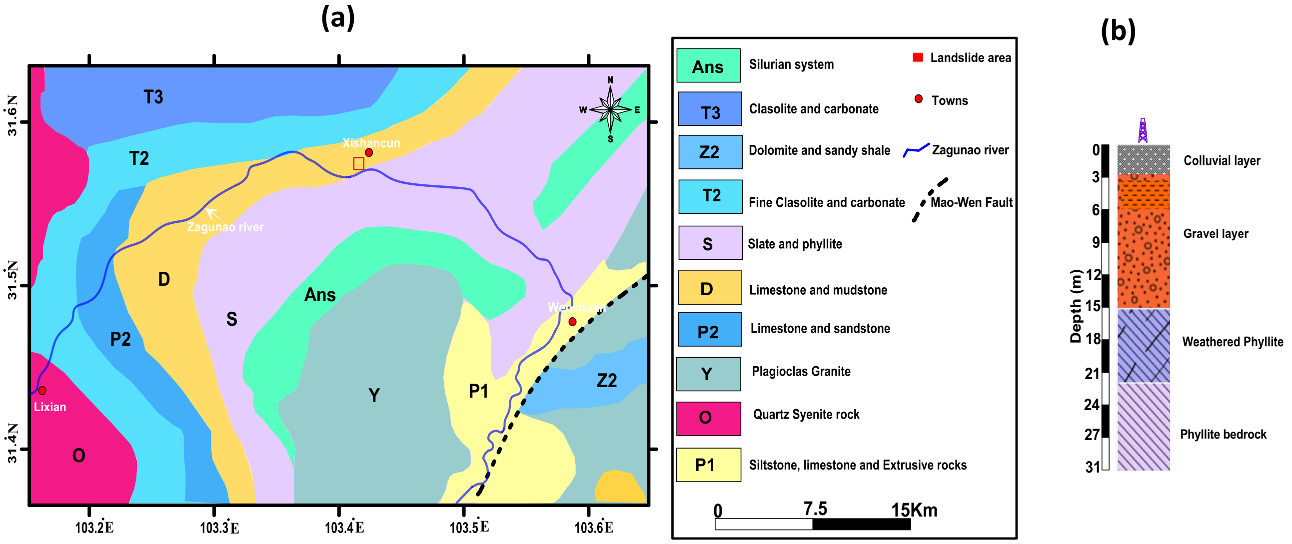

Figure 3: (a) Regional geological map of the study area with dominant lithologies, and (b) lithology portion of the research region and adjacent regions acquired from wells [24].

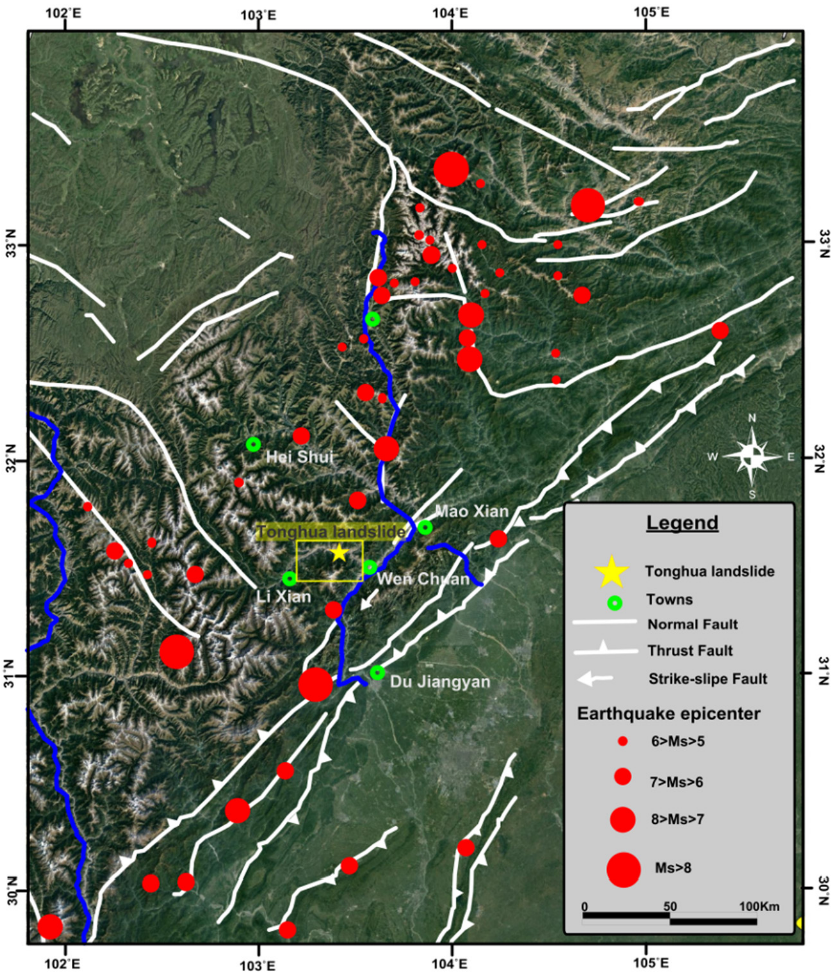

Figure 4: Locations of structural faults and seismic events around the Tonghua landslide modified from ref. [6].

specifically the Xishan County landslide, in the locality of the Tonghua landslip for many years (Figure 1).

2.2 MASW

MASW is an effective technique for high-resolution examination of surface and subsurface formations using functional resources. It has been used to tackle several tasks in geotechnical and environmental engineering, such as providing a planning basis [26], defining narrow fault regions [27–29], sensing cavities [30–33], seismic microzonation, site reaction experiments, and geotechnical characterization of substances close to the surface [34–36], and evaluating landslide strength [37]. Rayleigh wave signs were amassed using a single-ended irritation source layout and a collecting structure with geophones at points of different topographies. Inversion diffusion curves were computed using the frequency–wavenumber (F–K) assay to establish the variation of shear-wave velocity outlines with intensity. The probe strength of MASW is approximately related to $V_S/3f$, and the shear-wave velocity is susceptible to landslide distortion [35]. Recently, this assay has been used to identify two-dimensional (2D) and/or three-dimensional (3D) landslide structures [38,39].

The acquisition unit consists of a seismograph controlling 24-spike geophones with a frequency of 4.5 Hz and 2 m spacing, and a 6 kg iron hammer was used as a seismic source to generate wide-bandwidth exterior waves (Table 1) [40]. As shown in Figure 5, four (shear-wave velocity profiles of landslide debris SW-1, SW-2, SW-3, and SW-4) and an adjacent stable section were obtained using the surface wave method [26,34]. With the parameters used in this survey, shear-wave velocities at approximately 30 m depth could be obtained. Although the terrain in this region is rugged due to episodic landslide events, we planted the geophones in almost parallel and straight lines to ensure favorable conditions for the MASW survey. Special consideration was given to the parameters suggested in [41–43] to improve the data quality and avoid near-field

Table 1: Location, name, length, electrode/geophone spacing of 2D ERT and MASW profiles

Geophysical method	Location	Profile	Length (m)	Electrode/ geophone spacing (m)
ERT	Landslide debris	ERT1	124	4
		ERT2	124	4
		ERT3	124	4
		ERT4	124	4
		ERT5	124	4
		ERT6	240	5
	Stable relief	ERT7	124	4
MASW	Landslide debris	SW1	46	2
		SW2	46	2
		SW3	46	2
	Stable relief	SW4	46	2

effects. Data processing was finalized using the "SurfWave® 2020" following three main steps [37,44,45]. First, the dispersion curves were estimated by transforming each Rayleigh-wave shot fold (Figure 6a) to the frequency–phase velocity (f–V) domain for dispersion curve extraction (Figure 6b) [46]. Second, a one-dimensional (1D) S-wave velocity (V_s) profile (Figure 6c) was projected through the inversion process from the dispersion curve using a reiterative reversal algorithm functioning with the least-squares method inversion process to run automatically [40]. Similarly, an initial model, V_s, was generated by a mixture of numerous factors. The original model comprises 10 units, ensuring optimal resolution by iteratively using V_s.

In the preliminary model, V_s values and depth of access (Z_f) are chosen by assuming that V_s at a depth of Z_f is 1.09 times the measured phase velocity (C_f) at the frequency where wavelength λ_f [34], as expressed in the following equation:

$$Z_f = a\lambda_f, \tag{1}$$

where a is a coefficient that varies only slightly with frequency and is the result of extensive modeling.

Therefore, the maximum access strength imaged using the MASW method was usually monitored by the smallest regularity encountered while generating the initial model. Third, the MASW 1D shear-wave velocity outlines were gathered along with the study lines and then incorporated using the kriging algorithm to create 2D color grid shear-wave velocity profiles [26,31,47–49].

According to the National Earthquake Hazards Reduction Program (NEHRP) standards [50,51], V_s of the subsurface must be measured or estimated to a depth of approximately 30 m (V_{s30}) to study earthquake risks. It can be calculated using the following equation:

$$V_{s30} = \frac{\sum_{i-1}^{n} d_i}{\sum_{i-1}^{n} \frac{d_i}{V_{sf}}}, \tag{2}$$

where V_{s30} is the NEHRP SWV (seismic wave velocity), V_{sf} is the shear-wave velocity of any layer in m/s, and d_i is the thickness for any layer (0–30 m).

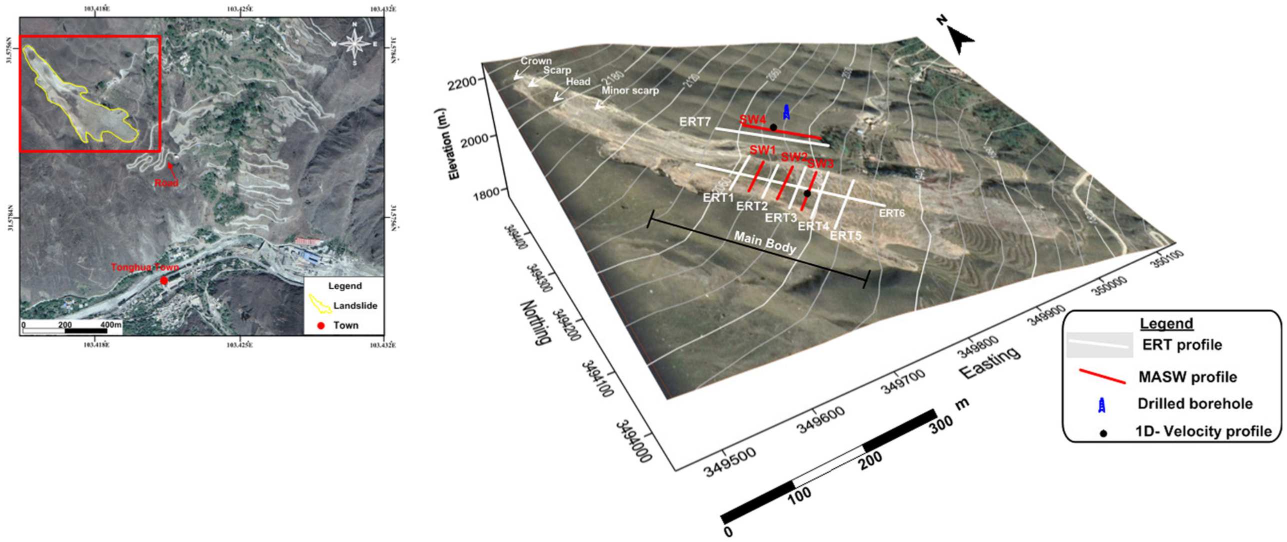

Figure 5: Digital elevation model of the Tonghua landslide overlaid by satellite view and locations of geophysical ERT and MASW data acquisition lines.

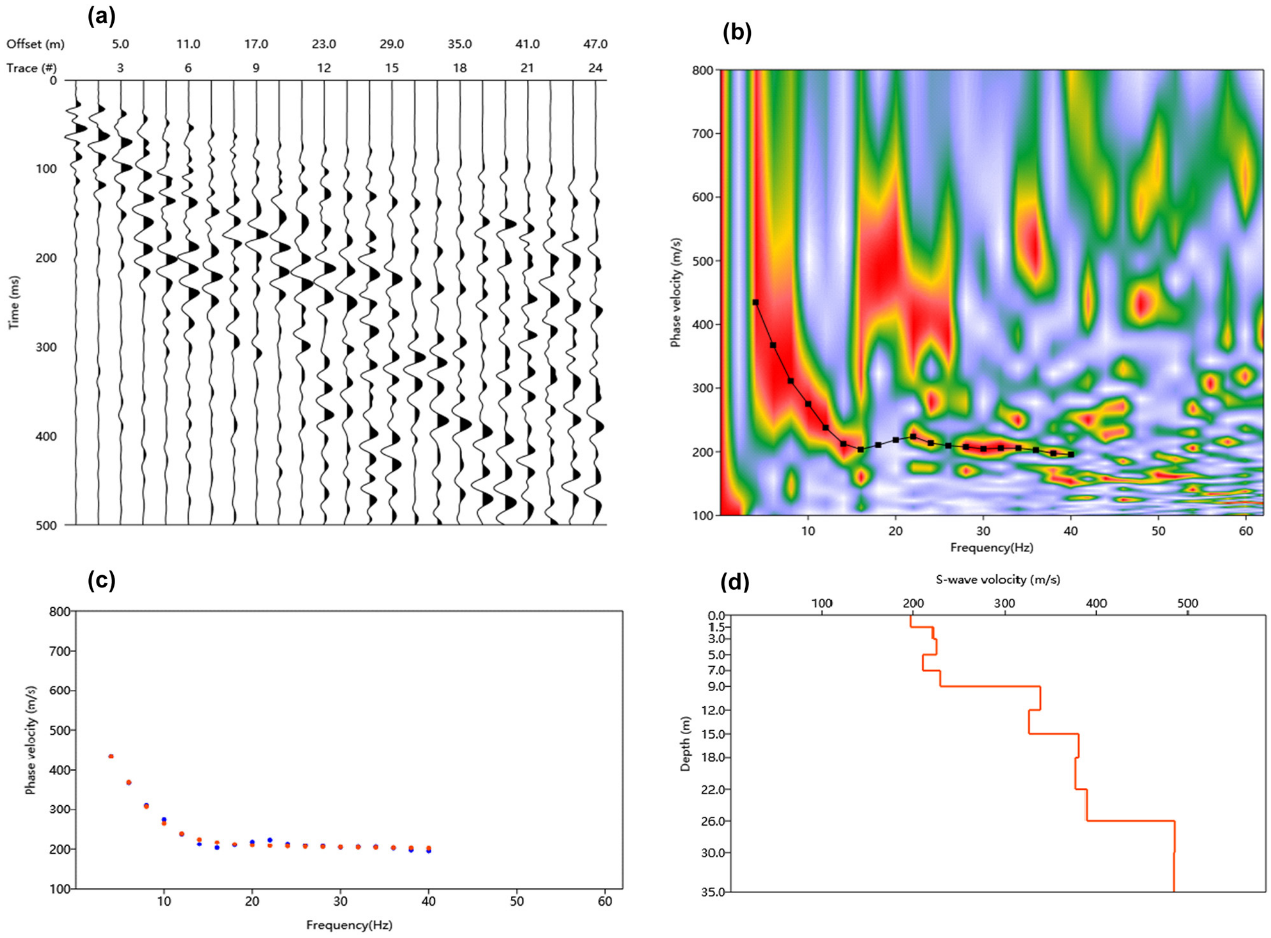

Figure 6: (a) Rayleigh-wave shot fold from SW-3, (b) the Rayleigh-wave dispersal image produced from (a), (c) experimental (red dotted line), theoretical (blue dotted line) dispersion curves, and (d) Shear wave velocity (S-velocity) construction using MASW data S-velocity estimate is exact down to the depth of about 26 m.

Table 2 lists the details of the landslide and its soil conditions based on the NEHRP standards [50]. The soil is classified into six types (A–F) based on their V_{s30}.

2.3 ERT

The ERT process produces an image of the allocations of highly saturated and clay-rich areas, showing low resistivity in the landslide, rock weathering, and fracturing [14,52–55]. Resistivity varies with the mineral elements, groundwater, and electrolytes in the subsurface layers [56]. In this method, a DC electrical current is injected into the subsurface. It runs through conductive media and is received by electrodes planted within the geophysical line [24]. 2D and 3D resistivity tomography methods are used to discover unstable slopes because they provide exact data on the electrical resistivity divisions and physical assets of geological structures [18,57].

Table 2: Soil type classification according to ref. [50]

NEHRP soil type	General description	Average V_{s30} (m/s)
A	Hard rock	>1,500
B	Rock	$760 < V_s \le 1{,}500$
C	Very dense soil and soft rock	$360 < V_s \le 760$
D	Stiff soil $15 \le N \le 50$ or $50\ \text{kPa} \le \text{Su} \le 100\ \text{kPa}$	$180 < V_s \le 360$
E	Soil or any profile with more than 3 m of soft clay defined as soil with PI > 20, w ≥ 40% and Su < 25 kPa	<180
F	Soils requiring site-specific evaluations	

Note: N: SPT blow count, Su: undrained shear strength, PI: plasticity index, w: water content.

For the Tonghua landslide, the electrical resistivity data were acquired using a multielectrode system (56 electrodes) with a SuperStingR8 (AGI-instruments) resistivity meter connected to a multicore cable. In this approach, ERT was used in different array lengths using a dipole–dipole electrode configuration to find variable investigation depths.

Several studies have been conducted using a dipole–dipole array for landslide investigation [13,58–60]. The main advantages of a dipole–dipole array include the following: (1) it is suitable for complex and deep-seated landslides; (2) it can determine isometric structures; and (3) it is sensitive to horizontal changes in resistivity [61]. The depth of this investigation was approximately 50 m. Data noise was evaluated using the stacking procedure [62]. Five to ten stacked electrical resistivity measurements were conducted for each point, and the resistivity meter automatically estimated the respective relative standard deviation. Resistivity was calculated using a standard deviation greater than 2%, and noticeable outliers were not considered.

Planning and arrangement of 3D electrode array operations on landslides at the desired depth were complicated and expensive. Although the sliding material was soft, the material distribution was not wide enough to set up a 3D array. A cost-effective alternative to true 3D ERT imaging is the pseudo-3D ERT imaging technique. This involves obtaining parallel and/or orthogonal surface 2D ERT profiles and processing them as though they are true 3D data [63,64].

Hence, seven 2D high-resolution survey profiles, including two longitudinal and five parallel transversal lines spread out on the landslide body, were obtained to investigate the landslide structure (Figure 5). The array length was 132–240 m with 4–5 m electrode spacing to increase the depth coverage, and the investigation depth ranged from 26 to 56 m (Table 1). Finally, the five traversal 2D sections were combined with reasonably accurate images of 3D structures. A statistical analysis of the determined apparent resistivity was performed after data collection to establish the frequency distribution.

The 2D ERT datasets were inverted using ResIPy software [65]. The code for resistivity inversion based on an objective regularized function was integrated with a weighted least-squares evaluation of the misfit (the solution type of Occam) after [66] adjustment for the imposed regularization constraints. To assess the accuracy of the numerical solution, a homogeneous earth structure was used to simulate forward models for different mesh discretization. The 2D ERT data inversion is a nonunique problem that needs constraints on the model structure to minimize possible solutions. An objective function connected to a linear system of equations was minimized to solve the tradeoff between the model constraints and the weighted data misfit [67,68].

Several factors can affect the imaging depth and resolution of the inverse model of electrical methods, including the amplitude of the signal relative to the conditions of ambient noise [69], parameterization type and regularization in the inversion, and geometry of the cables (number of segments, spacing between electrodes, number of electrodes, and type of array) [68].

The structure beneath the depth of investigation (DOI) should not be interpreted geologically. Therefore, estimates of the DOI for DC resistivity surveys are crucial when interpreting models obtained from any inversion. A statistical method developed in ref. [70] was employed to calculate a modified DOI index [71]. Two inversions with homogeneous reference models of different resistivity (0.1 and 10 times the logarithmic mean of the apparent resistivity values) were performed herein. To fit the values of the cumulative distribution of the calculated DOI index, the sum of two normal distributions was used, thus allowing the interpretability index to be calculated for each cell of the model. Another inversion was then performed with the mean of apparent resistivity (a third homogenous reference model). The interpretability index was an “alpha blending” step. To distinguish between poorly and well-constrained cells, the resistivity model was plotted specially.

3 Results and discussion

3.1 Deformation properties and landslide characterization

As shown in Figure 7(a) and (b), two cases of 1D V_s profiles were generated from MASW data (profiles SW3 and SW4) and correlated with existing boreholes using interval velocity functions. The boreholes near the survey lines were drilled by ref. [24], who investigated the Xishan village landslide. The two examples show a good match of the total rapidity from MASW with the stratigraphic logs. The contrast reveals that the top of the bedrock exterior has a shear-wave rapidity of more than 450 m/s. A comparison of MASW-1D profiles helped us to read the 2D V_s sections and debris depth.

The calculated velocity-depth 2D profiles of the earthflow debris showed a debris depth up to 30 m (Figure 8).

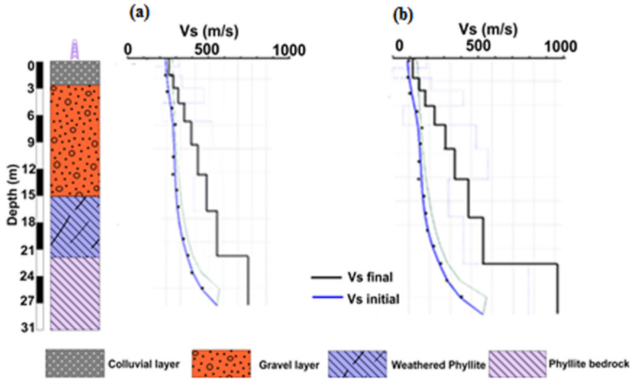

Figure 7: Matching 1D velocity profiles obtained from the MASW data to borehole logs situated in the investigated area. (a) 1D velocity profile SW4 was obtained from the stable slope section, and (b) 1D velocity profile SW3 was obtained from landslide debris.

After implementing a spatial interpolation approach, we could construct V_s slice maps at different depths [45]. The depth of the bedrock was obtained by comparing the V_s maps with borehole records (Figure 9). Furthermore, the low V_s encountered in the top 5–10 m of the debris indicates soft deposits or high clay content debris. Beneath this layer, the next horizon was a combination of high and low velocities, indicating several earlier episodes of landslides. The second layer exists in all three images (Figure 8(a), (c), and (d)) with high- to low-velocity contrasts. Visual interpretation confirmed the existence of small cavities and high weak zones, causing a collapse under worsening conditions and initiating debris movement. A relatively uniform layer of V_s (600–800 m/s) penetrating at a depth of 24–27 m was interpreted as the termination of debris deposits. It is considered a new slip surface for the existing debris.

The encountered rock masses have irregular dispersion with interactions between hard and soft rocks in the stable section. Generally, the fractured mechanical conditions of the geological stratum in this profile are vital for the overburden failure mechanisms. A combination of soft and hard rock layers and their residual bulk characteristics is evident in 2D sections. The overlying layers directly influenced the mechanical strength, failure

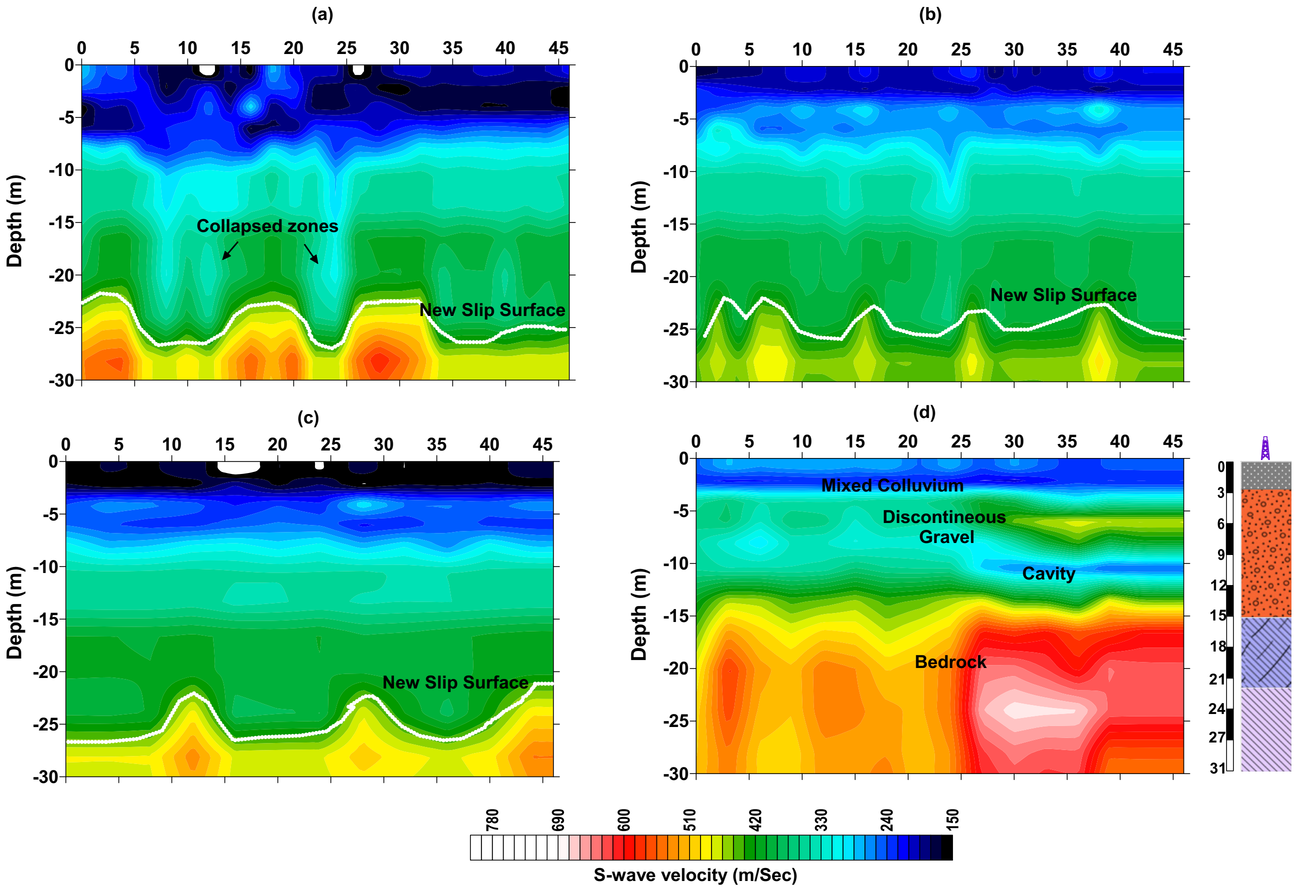

Figure 8: V_s 2D sections with the survey profiles. (a) Top of the debris (SW1); (b) at the middle (SW2); (c) at the trailing edge of the landslide debris (SW3); and (d) stable side beside the landslide site (SW4).

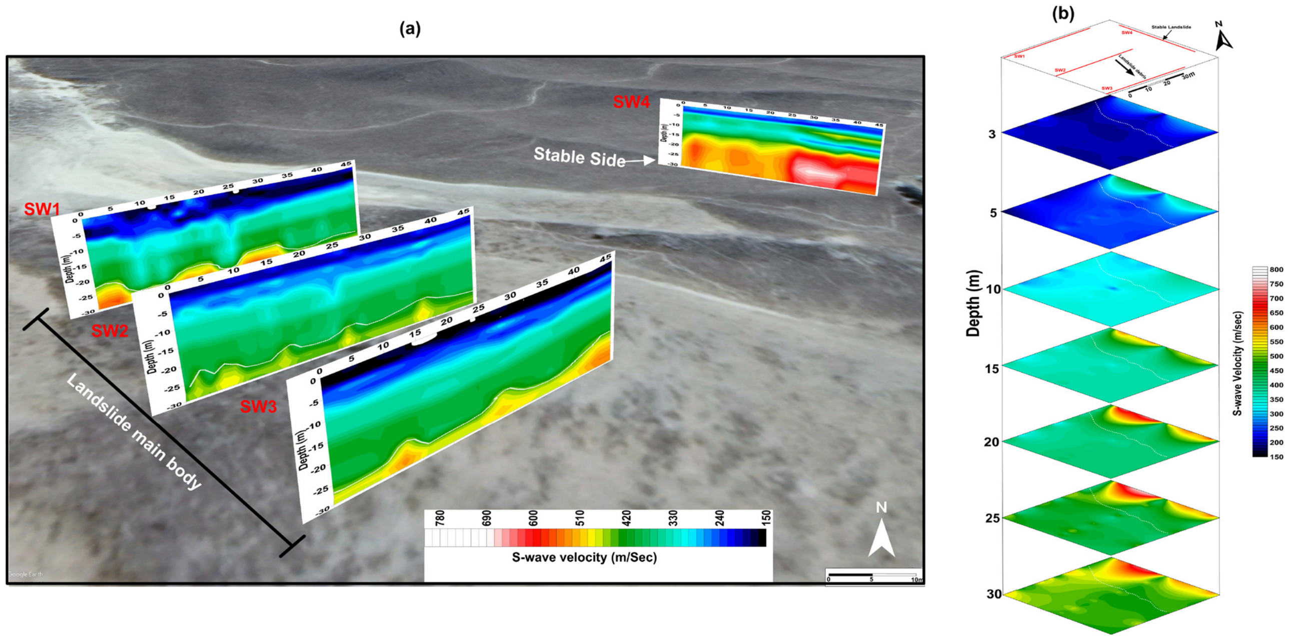

Figure 9: (a) 2D S-wave velocity sections projected onto Landsat image of Tongua landslide site (for locations, see Figure 5) and (b) S-wave velocity slicing maps illustrate the distribution of S-velocity at different depths.

mode, and residual bulk characteristics of the underlying rock stratum, as deduced from the visual interpretation of the lithological structure. Four geological layers were encountered in the study area based on the 2D sections after comparing with existing borehole logs from nearby areas and interpretation. The top colluvium layer is heterogeneous and contains rock fragments to a depth of 6–7 m. The next layer is 7–8 m thick and comprises altered gravel beds mixed with pebbles, and its velocity structures indicate a discontinuous depositional structure. The third layer is a low-velocity layer inserted between two high-velocity layers and depicts low velocities (150–200 m/s), representing high weathering conditions. This layer is interpreted as weathered phyllite that is 22 m deep. At the bottom, we found rocks with a velocity of 800–1,000 m/s. This is considered a bedrock for the examined slope.

According to the NEHRP standard, V_{s30} and soil types are classified into two soil classes (classes D and C) (Table 3).

Table 3: NEHRP site classification obtained from the MASW soil profiles of the study area

Profile	V_{s30} (m/s)	Soil classification (NEHRP)
SW-1	351	Type-D (stiff soil)
SW-2	332	Type-D (stiff soil)
SW-3	344	Type-D (stiff soil)
SW-4	482	Type-C (very dense soil and soft bedrock)

Soil class D was found in the landslide debris stiff soil, whereas class C was found mainly in the stable part of the slope as very dense soil and soft bedrock.

3.2 2D ERT profiles

Several 2D dipole–dipole measurements were conducted on the landslide debris and adjacent stable section. The array covering the stable and debris sections were 132 and 240 m long, respectively. The resistivity inversions achieved optimum estimations in seven repetitions, with less than 4% root-mean-square error. Figure 10a illustrates the 2D tomography ERT-6 profile performed longitudinally above the landslide debris. The debris basement at a depth of 40 m was highly conductive and extended up to 100 m. In the basement, the encountered values were less than 30 Ωm, making the conditions favorable for water saturation. Over the basement, the landslide-induced overlaid sediments contain low-to-high resistive materials of 80–250 Ωm. The debris-flow deposits showed an average thickness of approximately 20–25 m and were thicker in the central part. Intermittent areas with a resistivity of less than 20 Ωm were also found below the freshly accumulated sediment. These anomalous resistivity regions showed the locations of hidden clayey soil beneath the debris sediment. Water infiltration and fissure water runoff in the debris structure were also prominent. The DOI along this section

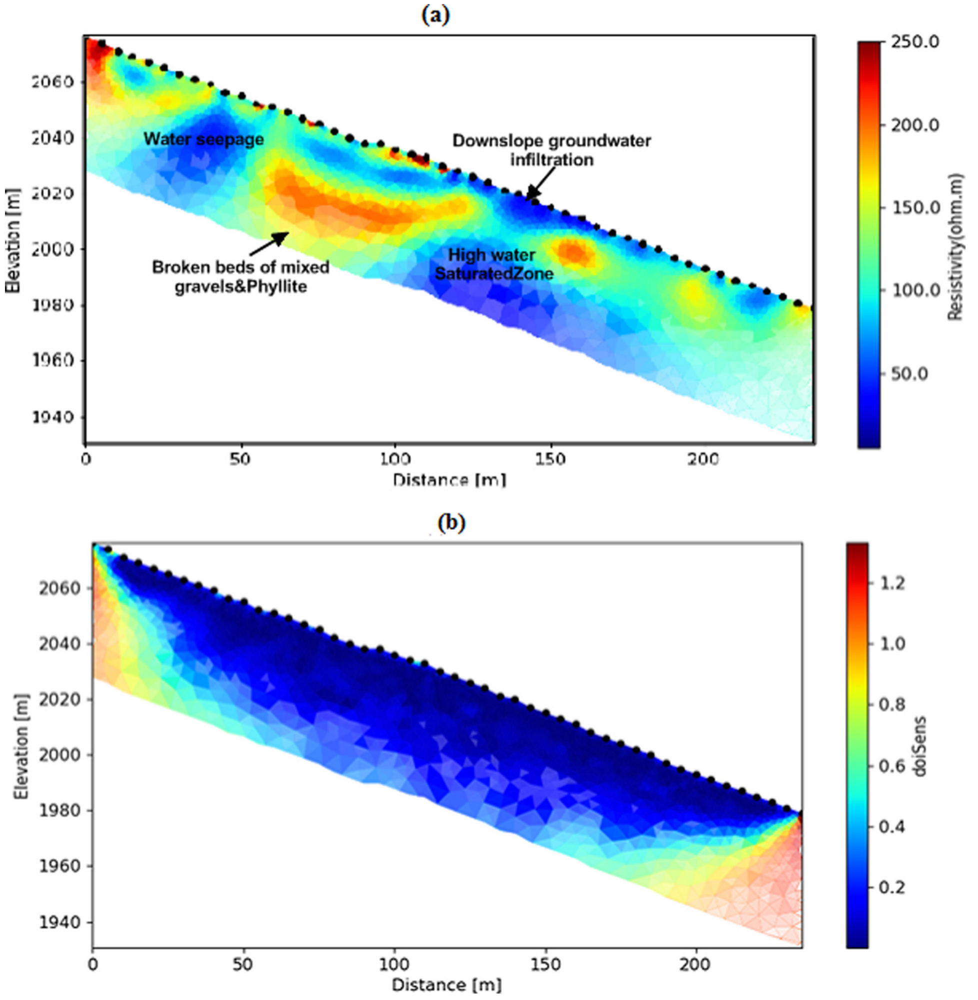

Figure 10: (a) ERT-6 profile crossing the main body of the landslide in the center with a spread length of 240 m and (b) DOI sensitivity sections show the adequate investigated depth.

ranged from 20 m at the edges of the section and line ends to 50 m at the profile center (Figure 10b).

We obtained the 2D ERT profile of the slope adjacent to the debris to understand its failure mechanism. This part of the hill was at the rear under a high debris load but did not move during the debris flow. The ERT-7 profile interpreted this relief as a bedrock outcrop with a resistivity greater than 250 Ωm (Figure 11a). After a 28–30 m-long continuous high-resistivity zone, a 90–95 m-long low-resistivity zone was observed. The low-resistivity region contained intermittent high-resistivity patches, which may be lenses of gravel or weathered phyllite. The stable relief also showed high water content at the toe end and can act as a slip initiator. Electrical resistivity reflects different factors, including the clay content porosity and water content. In general, different types of rocks have a wide range of electrical resistivity. Therefore, the values of electrical resistivity cannot be interpreted based on lithology. Thus, we compared our results with the literature [4,15,16] and nearby exploratory boreholes in the region. Based on the resistivity contrasts, three electrical resistivity ranges were assigned in the stable relief: (a) $\rho > 20\ \Omega\text{m}$ to surface water infiltration and fissure water runoff; (b) $\rho = 1\text{–}8\ \Omega\text{m}$ to the water-rich toe of the slope; and (c) $\rho > 250$ moist gravel and weathered phyllite. In this case, the active landslide material acts as an overburden beneath low-resistivity strata (5–200 Ωm). The active (lower) portion of the relief is classified into two extensive zones. The upper zone comprising displaced, relatively intact blocks (rafts) of bedrock, while the transitions into the lower zone indicate predominantly fractured materials with numerous closely spaced tension cracks and water-rich strata. On this basis, the new susceptible landslide may be classified as a block slide [72] or complex translational rockslide earthflow [73]. The DOI along this section ranges from 18 m at the edges and end lines of the section to 25 m at the profile center (Figure 11b).

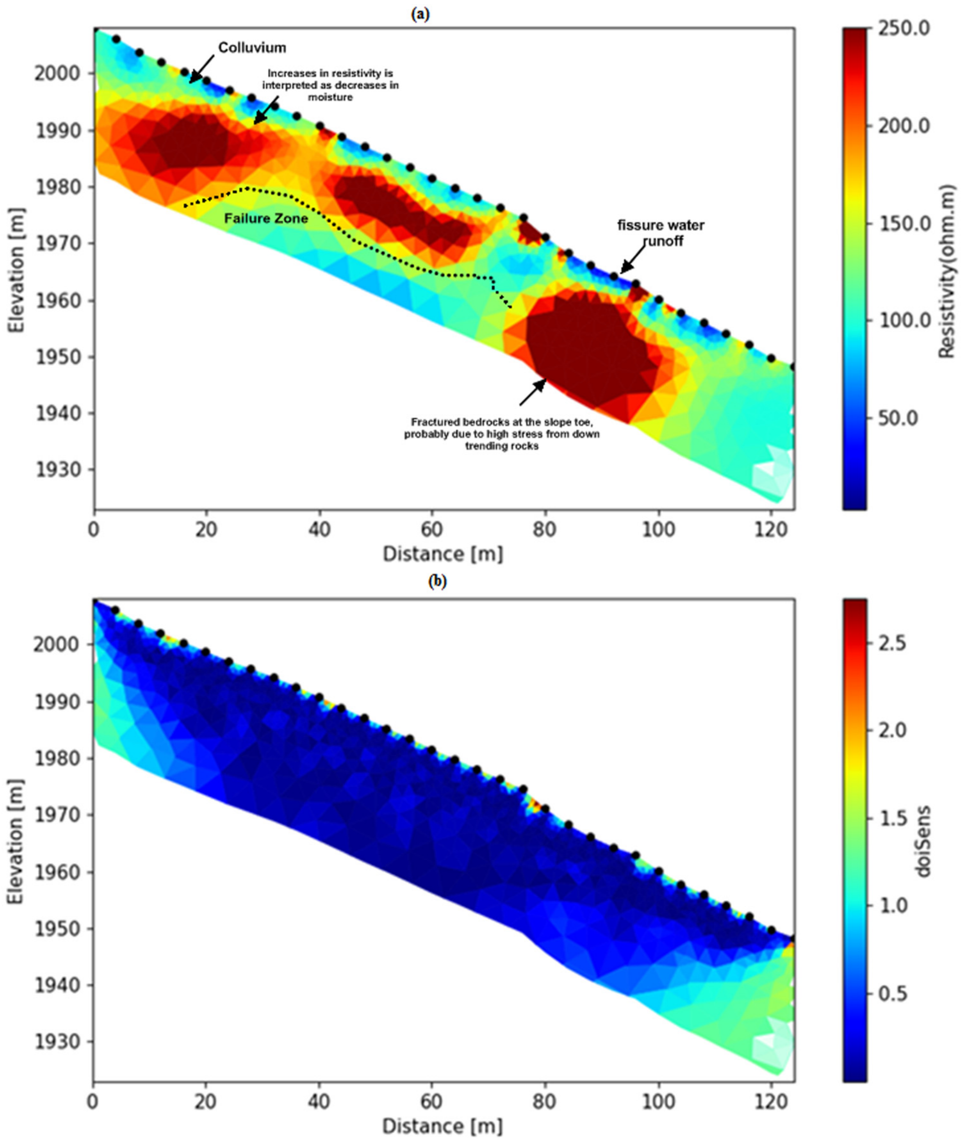

Figure 11: (a) Longitudinal ERT-7 profile, with a length of 124 m at the stable landslide section and (b) DOI sensitivity sections show the effective investigated depth.

3.3 Pseudo-3D inverted ERT model

To explore the influence of draining water out of the landslide debris, five 2D profile measurements were conducted and combined to construct pseudo-3D ERT using the obtained five parallel ERT profiles (Figure 12). The electrode spacing was 4 and 35 m in the *X*- and *Y*-axis, respectively. The 2D surveys had deeper exploration depths, lower noise, and simpler array geometry due to the longer array. Specific details about the conductive channels under the debris could be obtained from 3D measurements. Notably, the 2D array data for the inversion were used to construct a model that could summarize the connections of oversaturated drains (Figure 12). As shown in Figure 13(a), the locations with resistivity greater than 250 Ωm represent a lens of stiff deposits with low conductivity, corresponding to the expansion of previous debris movement. The 3D resistivity contour plot shows that the debris consists of three mixed layers: a stiff (dipping) layer with a high range of resistivity; a soft layer (the interim area) with a medium-resistivity range; and a low-resistivity layer, which is a highly saturated stratum. Figure 13(c) shows the 3D volume extraction of resistivity below 30 Ωm and outlines a prominent conductive zone beneath the hard deposits. The clear separation of these two resistivity volumes confirms the water flow paths and results from the perching of rainwater draining through the debris. The unconsolidated layer above the saturated layer exhibits medium resistivity of 80–190 Ωm. A medium-resistivity volume surrounds the

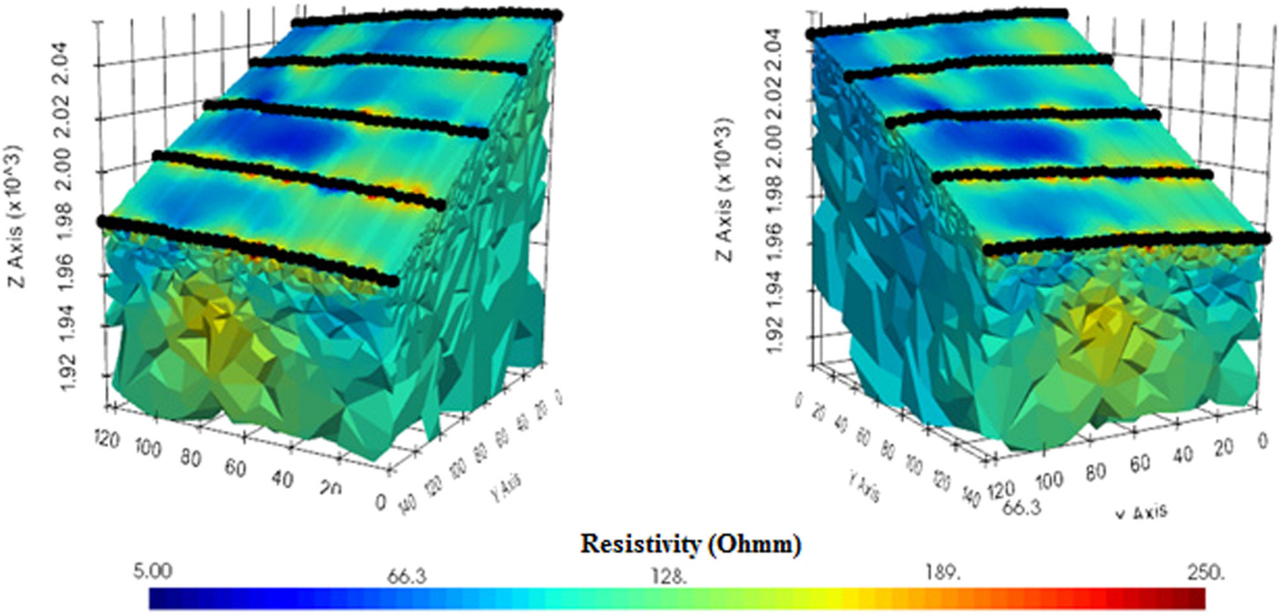

Figure 12: Pseudo-3D inverted ERT model built from combined 3D inversion of parallel ERT-1, ERT-2, ERT-3, ERT-4, and ERT-5 profiles, crossing the debris transversely, almost 25–30 m below the topographic surface. The high distribution of low-resistivity values (blue color) shows the pathways created by infiltrating water.

phyllite deposits at the interface with compaction. The drilling record confirms that the resistivity of pebbly clay in this region varies from 50 to 200 Ωm [24]. This unconsolidated stratum is a mixture of slit, pebbly clay, and colluvium. The high resistivity is widely distributed within the medium-resistivity region (200–250 Ωm). These deposits cover the slope

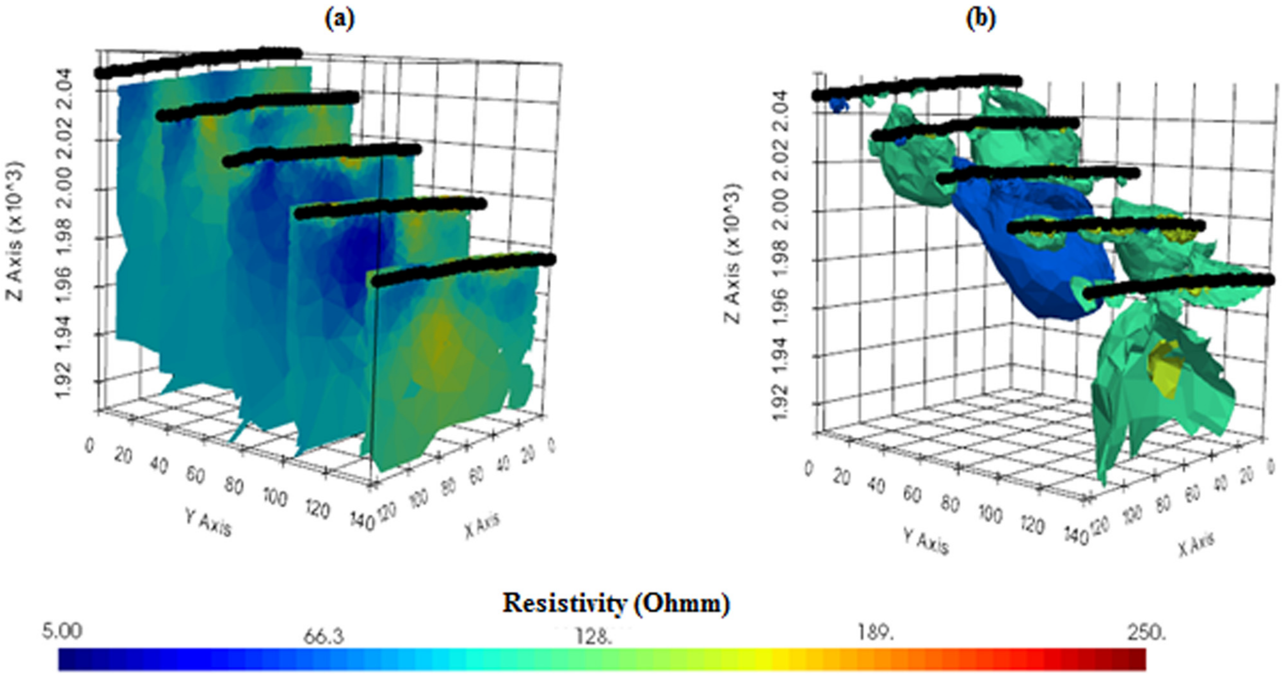

Figure 13: (a) Represents the inverted results by combining 2D parallel ERT lines to create a 3D slice in the *X* and *Y* axes with reasonable RMS error; (b) the 3D inverted image represents the overall status of the debris with core leaking zones of low-resistivity (<20 Ωm) and high-resistivity (>250 Ωm) and represents the volumetric contrasts between extremely hard and saturated debris strata and the volume of debris that is highly saturated with water.

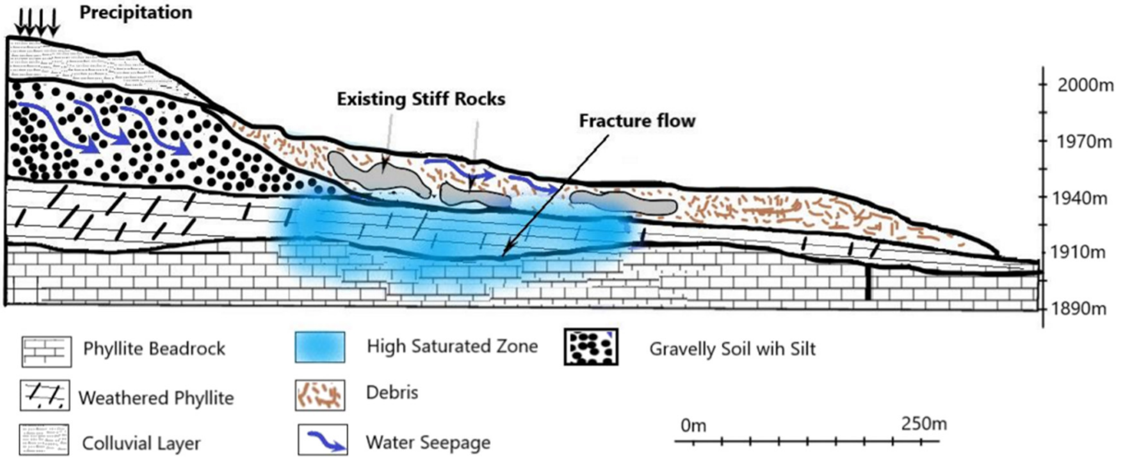

Figure 14: A typical situation of the Tonghua Village landslide, the best-fit model, developed after the geophysical investigation, with prominent lithology and water saturation zone.

until the trailing edge and make them vulnerable to the steepness of the slope.

3.4 Landslide development and hydrogeological model

In this study, the spread length of MASW was 46 m, which could limit the shear-wave velocity estimation to a particular depth. The obtained MASW profiles have soil deposits approximately 30 m thick. The landslide was characterized as a zone covering class D bearing, very dense soil, and soft rocks. A visual inspection of the MASW survey revealed well-defined soil and rock characteristics when mapping the shallow 2–30 m deep. At this depth, the shear-wave velocity was attained with fair accuracy in signal processing by preserving the low frequencies (high wavelengths) for deeper penetrations. The geotechnical characteristics of the study area can be used for preliminary design of new buildings. However, laboratory experiments are needed to estimate the friction angles and deformation moduli at certain locations, guided by the conventional relationship between the seepage field and landslide stiffness through the MASW and ERT characteristics. We developed a schematic model of the landslide main body and its hydrogeological features in the study area based on the integrated results of ERT and MASW. The evolution of the landslide was consistent with the hydrogeological features (Figure 14).

After the landslide, the adjacent slope was strongly deformed. Potential preferential flow paths were developed and formed by fractured zones, scarps, cracks, and fissures. Thus, much of the recharged groundwater infiltrates and accumulates under the deposited landslide mass. The slope toe is dry and does not drain water as runoff, causing gradual erosion and softening of the debris basement. An increase in the surface runoff and a decrease in the discharge capacity can act as reactivation factors. On the other hand, in the stable slope, the interflow of gravelly soil was not visible in the ERT-7 profile (Figure 11) due to the steepness of the slope. The surface runoff dominates the infiltration replenishment and erodes the gravel top layer in the exposed outcrops of the bedrock slopes. Thus, the absence of overlying colluvium and pebbly clay layers in the surrounding areas requires landslide susceptibility assessment. The sliding beds or moderately weathered bedrock layers on the slopes are greatly affected by the direct infiltration due to the absence of overlying colluvium layers. Hence, the landslide gradually deformed with time and finally collapsed. The trailing edge of the landslide was approximately 200 m wide and followed a steep slope with a depression angle of 25–35°. Currently, the saturated zone comprises a significant portion of the measured volume of the debris. Hence, oversaturation can cause the debris to move again.

4 Conclusion

In this study, we evaluated the current dynamics and hydrogeological conditions of landslide debris and adjacent stable slopes through seismic and electrical measurements using the Tonghua landslide site in China as a case study. These measurements provided excellent results for both the stable and displaced sections of the slope. The debris was stable under current stress and groundwater conditions, and its trailing edge was more than 200 m wide and contains the first episodic hard rock layer of landslide deposits with cracks and voids. The current saturation level can remain stable until it reaches the maximum saturation level. Fissure flow has not yet been detected at the trailing edge of the debris, indicating high seasonal variations, which may reactivate the landslide by increasing the volumetric water content. On the other hand, the seismic survey classified the area as a dense type with soft rocks. The combined geophysical investigations could aid *in situ* delineation of groundwater infiltration paths in the debris deposits. The results of this investigation can provide valuable guidance for selecting the positions of drainage channels or flumes.

Abbreviations

ERT	electrical resistivity tomography
DOI	depth of investigation
MASW	multichannel analysis of surface waves
NEHRP	national earthquake hazards reduction program

Acknowledgments: Sincere thanks and gratitude to the Researchers Supporting Project number (RSP-2021/351), King Saud University, Riyadh, Saudi Arabia, for funding this research article. Also, we would like to thank Dr. Binbin Mi, Earth Science School of Zhejiang University, for his generous help in processing and interpreting the MASW data and Prof. Andrew Binley, Lancaster University and James Boyd for helping in ERT data inversion. We wish to thank the anonymous reviewers for their careful reading and providing valuable comments to improve the initial version of this paper.

Author contributions: This work was made possible by significant contributions from all authors: conceptualization, A.A.E., I.I.; methodology (ERT and MASW); software, A.A.E.; validation, I.I. and O.M.O.; formal analysis, A.A.E.; investigation, I.I.; data curation, I.I.; writing – original draft preparation, A.E. and I.I.; writing – review and editing, A.E., J.M.; visualization A.A.E., I.I., K.A., H.A. and O.M.O. All authors have read and agreed to the published version of the manuscript.

Conflict of interest: Authors state no conflict of interest.

Data availability statement: The data are not publicity distributed because of privacy of researchers. Therefore, the data supporting the present study results are available from the corresponding author upon reasonable request.

References

[1] Cui P. Progress and prospects in research on mountain hazards in China. Prog Geogr. 2014;33:145–52.
[2] Bortolozo CA, Motta MFB, Andrade MRM, Lavalle LVA, Mendes RM, Simões SJC, et al. Combined analysis of electrical and electromagnetic methods with geotechnical soundings and soil characterization as applied to a landslide study in Campos do Jordão City, Brazil. J Appl Geophys. 2019;161:1–14.
[3] Runqiu H, Weile L. Formation, distribution and risk control of landslides in China. J Rock Mech Geotech Eng. 2011;3:97–116.
[4] Crawford MM, Bryson LS. Assessment of active landslides using field electrical measurements. Eng Geol. 2018;233:146–59.
[5] Ling C, Xu Q, Zhang Q, Ran J, Lv H. Application of electrical resistivity tomography for investigating the internal structure of a translational landslide and characterizing its groundwater circulation (Kualiangzi landslide, Southwest China). J Appl Geophys. 2016;131:154–62.
[6] Chen K, Lang H, Wang L, Liu K, Zhou Y, Mi M. Failure mechanisms and deformation processes of a high-locality landslide at Tonghua Town, Li County, China, 2017. Landslides. 2020;17:165–77.
[7] Imani P, Tian G, El-Raouf AA. Assessment of spatiotemporal changes in water contents of landslide zone by geophysical methods: a case study. Arab J Geosci. 2021;14:1380. doi: 10.1007/s12517-021-07768-y. Epub ahead of print.
[8] McCann D, Forster A. Reconnaissance geophysical methods in landslide investigations. Eng Geol. 1990;29:59–78.
[9] Perrone A, Lapenna V, Piscitelli S. Electrical resistivity tomography technique for landslide investigation: a review. Earth-Sci Rev. 2014;135:65–82.
[10] Keskinsezer A, Dağ E. Investigating of soil features and landslide risk in Western-Atakent (İstanbul) using resistivity, MASW, Microtremor and boreholes methods. Open Geosci. 2019;11:1112–28.
[11] Leppänen JJ, Saarinen T, Jilbert T, Oulasvirta P. Near-surface seismic refraction tomography and MASW for site characterization in Phuentsholing. Bhutan Himalaya SN Appl Sci. 2021;3:1–18.
[12] Capizzi P, Martorana R. Integration of constrained electrical and seismic tomographies to study the landslide affecting the cathedral of Agrigento. J Geophys Eng. 2014;11:045009.
[13] Donohue S, Long M, O-Connor P, Eide Helle T, Aspmo Pfaffhuber A, Rømoen M. Multi-method geophysical mapping of quick clay. Surf Geophys. 2012;10:207–19.
[14] Imani P, Tian G, Hadiloo S, El-Raouf AA. Application of combined electrical resistivity tomography (ERT) and seismic refraction tomography (SRT) methods to investigate Xiaoshan district landslide site: Hangzhou, China. J Appl Geophys. 2021;184:104236. doi: 10.1016/j.jappgeo.2020.104236. Epub ahead of print.
[15] Perrone A, Canora F, Calamita G, Bellanova J, Serlenga V, Panebianco S, et al. A multidisciplinary approach for landslide residual risk assessment: the Pomarico landslide (Basilicata

Region, Southern Italy) case study. Landslides. 2021;18:353–65.

[16] Marciniak A, Kowalczyk S, Gontar T, Owoc B, Nawrot A, Luks B, et al. Integrated geophysical imaging of a mountain landslide – a case study from the Outer Carpathians, Poland. J Appl Geophys. 2021;191:104364.

[17] Cevasco A, Termini F, Valentino R, Meisina C, Bonì R, Bordoni M, et al. Residual mechanisms and kinematics of the relict Lemeglio coastal landslide (Liguria, northwestern Italy). Geomorphology. 2018;320:64–81.

[18] Chang P-Y, Chen C, Chang S-K, Wang TB, Wang CY, Hsu SK. An investigation into the debris flow induced by Typhoon Morakot in the Siaolin Area, Southern Taiwan, using the electrical resistivity imaging method. Geophys J Int. 2012;188:1012–24.

[19] Crawford MM, Bryson LS, Woolery EW, Wang Z. Using 2-D electrical resistivity imaging for joint geophysical and geotechnical characterization of shallow landslides. J Appl Geophys. 2018;157:37–46.

[20] Gance J, Malet J-P, Supper R, Sailhac P, Ottowitz D, Jochum B. Permanent electrical resistivity measurements for monitoring water circulation in clayey landslides. J Appl Geophys. 2016;126:98–115.

[21] Jianliang W, Iqbal I, Sanxi P, Yang Y, Jie L, Tianyu Z. Integrated geophysical survey in defining subsidence features of Glauber's Salt Mine, Gansu Province in China. Geotech Geol Eng. 2021;39:1–10.

[22] Mreyen A-S, Cauchie L, Micu M, Onaca A, Havenith HB. Multiple geophysical investigations to characterize massive slope failure deposits: application to the Balta rockslide, Carpathians. Geophys J Int. 2021;225:1032–47.

[23] Del Gaudio V, Wasowski J, Hu W, Capone P, Venisti N, Li Y. Ambient noise and ERT data provide insights into the structure of co-seismic rock avalanche deposits in Sichuan (China). Bull Eng Geol Environ. 2021;80:1–18.

[24] Su L, Xu X, Geng X, Liang S. An integrated geophysical approach for investigating hydro-geological characteristics of a debris landslide in the Wenchuan earthquake area. Eng Geol. 2017;219:52–63.

[25] Xu D, Hu X-Y, Shan C-L, Li RH. Landslide monitoring in southwestern China via time-lapse electrical resistivity tomography. Appl Geophys. 2016;13:1–12.

[26] Miller RD, Xia J, Park CB, Ivanov JM. Multichannel analysis of surface waves to map bedrock. Lead Edge. 1999;18:1392–6.

[27] de Almeida SF, de Sousa LB, Vieira LA, Chiamollera MI, Barros Jde N. Delineating a shallow fault zone and dipping bedrock strata using multichannel analysis of surface waves with a land streamer. Geophysics. 2006;71(5):789–93. doi: 10.1190/1.2227521. Epub ahead of print.

[28] Yilmaz Ö, Eser M, Berilgen M. A case study of seismic zonation in municipal areas. Lead Edge. 2006;25:319–30.

[29] Ikeda T, Tsuji T, Matsuoka T. Window-controlled CMP crosscorrelation analysis for surface waves in laterally heterogeneous media. Geophysics. 2013;78(6):95–105. doi: 10.1190/geo2013-0010.1. Epub ahead of print.

[30] Xia J, Chen C, Li PH, Lewis MJ. Delineation of a collapse feature in a noisy environment using a multichannel surface wave technique. Geotechnique. 2004;54:17–27.

[31] Xia J, Chen C, Tian G, Miller RD, Ivanov J. Resolution of high-frequency Rayleigh-wave data. J Environ Eng Geophys. 2005;10:99–110.

[32] Sloan SD, Peterie SL, Miller RD, Ivanov J, Schwenk JT, McKenna JR. Detecting clandestine tunnels using near-surface seismic techniques. Geophysics. 2015;80:EN127–35.

[33] Schwenk JT, Sloan SD, Ivanov J, Miller RD. Surface-wave methods for anomaly detection. Geophysics. 2016;81:EN29–42.

[34] Park CB, Miller RD, Xia J. Multichannel analysis of surface waves. Geophysics. 1999;64:800–8.

[35] Jongmans D, Bièvre G, Renalier F, Schwartz S, Beaurez N, Orengo Y. Geophysical investigation of a large landslide in glaciolacustrine clays in the Trièves area (French Alps). Eng Geol. 2009;109:45–56.

[36] Anbazhagan S, Subramanian S, Yang X. Geoinformatics in applied geomorphology. London: CRC Press, Taylor and Francis Group; 2011. p. 397.

[37] Mi B, Xia J, Shen C, Wang L, Hu Y, Cheng F. Horizontal resolution of multichannel analysis of surface waves. Geophysics. 2017;82:EN51–66.

[38] Grandjean G, Gourry J-C, Sanchez O, Bitri A, Garambois S. Structural study of the Ballandaz landslide (French Alps) using geophysical imagery. J Appl Geophys. 2011;75:531–42.

[39] Júnior SBL, Prado RL, Mendes RM. Application of multichannel analysis of surface waves method (MASW) in an area susceptible to landslide at Ubatuba City, Brazil. Rev Bras Geofis. 2012;30(2):213–24.

[40] Xia J, Miller RD, Park CB. Estimation of near-surface shear-wave velocity by inversion of Rayleigh waves. Geophysics. 1999;64:691–700.

[41] Roy N, Jakka RS. Near-field effects on site characterization using MASW technique. Soil Dyn Earthq Eng. 2017;97:289–303.

[42] Yoon S, Rix GJ. Near-field effects on array-based surface wave methods with active sources. J Geotech Geoenviron Eng. 2009;135:399–406.

[43] Zeng C, Xia J, Miller RD, Tsoflias GP, Wang Z. Numerical investigation of MASW applications in presence of surface topography. J Appl Geophys. 2012;84:52–60.

[44] Mi B, Xia J, Shen C, Wang L. Dispersion energy analysis of Rayleigh and Love waves in the presence of low-velocity layers in near-surface seismic surveys. Surv Geophys. 2018;39:271–88.

[45] Mi B, Xia J, Bradford JH, Shen C. Estimating near-surface shear-wave-velocity structures via multichannel analysis of Rayleigh and love waves: An experiment at the Boise hydrogeophysical research site. Surv Geophys. 2020;41:323–41.

[46] Park CB, Miller RD, Xia J. Imaging dispersion curves of surface waves on multi-channel record. SEG Technical Program Expanded Abstracts. 1998;17(1):1377–80.

[47] Matheron G. Principles of geostatistics. Econ Geol. 1963;58:1246–66.

[48] Xia J, Miller RD, Park CB, Hunter JA, Harris JB. Comparing shear-wave velocity profiles from MASW with borehole measurements in unconsolidated sediments, Fraser River Delta, BC, Canada. J Environ Eng Geophys. 2000;5:1–13.

[49] Luo Y, Xia J, Liu J, Xu Y, Liu Q. Research on the middle-of-receiver-spread assumption of the MASW method. Soil Dyn Earthq Eng. 2009;29:71–9.

[50] Council (BSSC) BSS. Nehrp recommended seismic provisions for new buildings and other structures (fema p-750). Report

Prepared for the Federal Emergency Management Agency (FEMA).

[51] Thitimakorn T, Raenak T. NEHRP site classification and preliminary soil amplification maps of Lamphun City, Northern Thailand. Open Geosci. 2016;8:538–47.

[52] Göktürkler G, Balkaya Ç, Erhan Z. Geophysical investigation of a landslide: the Altındağ landslide site, İzmir (western Turkey). J Appl Geophys. 2008;65:84–96.

[53] Lebourg T, Binet S, Tric E, Jomard H, El Bedoui S. Geophysical survey to estimate the 3D sliding surface and the 4D evolution of the water pressure on part of a deep seated landslide. Terra Nova. 2005;17:399–406.

[54] Naudet V, Lazzari M, Perrone A, Loperte A, Piscitelli S, Lapenna V. Integrated geophysical and geomorphological approach to investigate the snowmelt-triggered landslide of Bosco Piccolo village (Basilicata, southern Italy). Eng Geol. 2008;98:156–67.

[55] Bellanova J, Calamita G, Giocoli A, Luongo R, Macchiato M, Perrone A, et al. Electrical resistivity imaging for the characterization of the Montaguto landslide (southern Italy). Eng Geol. 2018;243:272–81.

[56] Telford WM, Telford W, Geldart L, Geldart LP, Sheriff RE. Applied geophysics. 2nd ed. Cambridge university press; 1990. p. 792. ISBN: 9781139167932, https://doi.org/10.1017/CBO9781139167932.

[57] Green AG, Maurer H, Spillmann T, Heincke B, Willenberg H. High-resolution geophysical techniques for improving hazard assessments of unstable rock slopes. Lead Edge. 2006;25(3):311–6.

[58] Jardani A, Revil A, Dupont J-P. Stochastic joint inversion of hydrogeophysical data for salt tracer test monitoring and hydraulic conductivity imaging. Adv water Resour. 2013;52:62–77.

[59] Reynolds JM. An introduction to applied and environmental geophysics. John Wiley & Sons; 2011. p. 710. ISBN: 978-0-470-97544-2, https://www.wiley.com/en-eg/An+Introduction+to+Applied+and+Environmental+Geophysics%2C+2nd+Edition-p-9780470975442.

[60] Mita M, Glazer M, Kaczmarzy R, Dąbrowski M, Mita K. Case study of electrical resistivity tomography measurements used in landslides investigation, Southern Poland. Contemp Trends Geosci. 2018;7(1):110–26.

[61] Falae PO, Kanungo DP, Chauhan PKS, Dash RK. Electrical resistivity tomography (ERT) based subsurface characterisation of Pakhi Landslide, Garhwal Himalayas, India. Environ Earth Sci. 2019;78:1–18.

[62] Robert T, Dassargues A, Brouyère S, Kaufmann O, Hallet V, Nguyen F. Assessing the contribution of electrical resistivity tomography (ERT) and self-potential (SP) methods for a water well drilling program in fractured/karstified limestones. J Appl Geophys. 2011;75:42–53.

[63] Yi M-J, Kim J-H, Song Y, Cho SJ, Chung SH, Suh JH. Three-dimensional imaging of subsurface structures using resistivity data. Geophys Prospect. 2001;49:483–97.

[64] Chambers J, Ogilvy R, Kuras O, Cripps J, Meldrum P. 3D electrical imaging of known targets at a controlled environmental test site. Environ Geol. 2002;41:690–704.

[65] Blanchy G, Saneiyan S, Boyd J, McLachlan P, Binley A. ResIPy, an intuitive open source software for complex geoelectrical inversion/modeling. Comput Geosci. 2020;137:104423.

[66] Constable S, Parker K, Constable C. Occam's inversion a practical algorithm for generating smooth models from EM sounding data. Geophysics. 1987;52:289–300.

[67] Backus G, Gilbert F. The resolving power of gross earth data. Geophys J Int. 1968;16:169–205.

[68] Binley A, Kemna A. DC resistivity and induced polarization methods. Amsterdam: Elsevier; 2005.

[69] Day-Lewis FD, Singha K, Binley AM. Applying petrophysical models to radar travel time and electrical resistivity tomograms: Resolution-dependent limitations. J Geophys Res Solid Earth. 2005;110:B08206.

[70] Deceuster J, Etienne A, Robert T, Nguyen F, Kaufmann O. A modified DOI-based method to statistically estimate the depth of investigation of dc resistivity surveys. J Appl Geophys. 2014;103:172–85.

[71] Oldenburg DW, Li Y. Estimating depth of investigation in dc resistivity and IP surveys. Geophys. 1999;64:403–16.

[72] Panet M. Discussion of KW John's paper (ASCE proc. paper 5865, March 1968). J Soil Mech Found Div. 1969;95:685–6.

[73] Cruden DM, Varnes DJ. Landslide types and processes, special report 247. Transportation Research Board, U.S. National Academy of Sciences; 1996;247:36–57.